Published in final edited form as:
J Mol Cell Cardiol. 2016 April ; 93: 32–43. doi:10.1016/j.yjmcc.2016.02.012.

Oxidative stress decreases microtubule growth and stability in ventricular myocytes

Benjamin M. L. Drum[1], **Can Yuan**[1], **Lei Li**[1], **Qinghang Liu**[1], **Linda Wordeman**[1], and **L. Fernando Santana**[2]

[1]Department of Physiology & Biophysics, University of Washington School of Medicine, Seattle, Washington, 98195

[2]Deparment of Physiology & Membrane Biology, University of California School of Medicine, Davis, California, 95616

Abstract

Microtubules (MTs) have many roles in ventricular myocytes, including structural stability, morphological integrity, and protein trafficking. However, despite their functional importance, dynamic MTs had never been visualized in living adult myocytes. Using adeno-associated viral vectors expressing the MT-associated protein plus end binding protein 3 (EB3) tagged with EGFP, we were able to perform live imaging and thus capture and quantify MT dynamics in ventricular myocytes in real time under physiological conditions. Super-resolution nanoscopy revealed that EB1 associated in puncta along the length of MTs in ventricular myocytes. The vast (~80%) majority of MTs grew perpendicular to T-tubules at a rate of 0.06 $\mu m*s^{-1}$ and growth was preferentially (82%) confined to a single sarcomere. Microtubule catastrophe rate was lower near the Z-line than M-line. Hydrogen peroxide increased the rate of catastrophe of MTs ~7-fold, suggesting that oxidative stress destabilizes these structures in ventricular myocytes. We also quantified MT dynamics after myocardial infarction (MI), a pathological condition associated with increased production of reactive oxygen species (ROS). Our data indicate that the catastrophe rate of MTs increases following MI. This contributed to decreased transient outward K^+ currents by decreasing the surface expression of $K_v4.2$ and $K_v4.3$ channels after MI. On the basis of these data, we conclude that, under physiological conditions, MT growth is directionally biased and that increased ROS production during MI disrupts MT dynamics, decreasing K^+ channel trafficking.

Keywords

microtubule dynamics; cardiomyocytes; live imaging; oxidative stress; myocardial infarction; transient outward current

---

Contact information: Luis F. Santana, Phone: 530-752-8836, lfsantana@ucdavis.edu.

Disclosures
None.

1. Introduction

Microtubules (MTs) are cytoskeletal fibers formed by the polymerization of αβ tubulin dimers. They have several functions in cellular processes, such as sustaining cell shape, mitosis, and intracellular trafficking of proteins [1]. In mature non-differentiating ventricular myocytes, MTs cannot play a role in mitosis, but still maintain important functions in the cell [2]. MTs are dynamically active and switch between phases of growth and shrinking, a process called dynamic instability [3]. MT dynamics can be characterized by measuring the growth rate and shrinkage rate, as well as the frequency of catastrophe (i.e., the transition from growth to shrinkage) and rescue (i.e., the transition from shrinkage to growth) [4]. Although MTs have been visualized in fixed tissue, they have not been seen assembling in live cardiac myocytes.

Plus-end binding (EB) proteins constitute a unique group of structurally and functionally diverse proteins that target the plus ends of growing MTs. These proteins orchestrate MT growth and recruit MT regulators. EBs are also implicated in MT-based transport [5, 6]. EBs autonomously track growing MT ends and are involved in many MT-based processes [7]. Three EB (EB1-3) isoforms have been identified to date. Of these proteins, EB1 (30 kDa) has previously been identified as expressed in the heart [8].

The formation of reactive oxidative species (ROS) has been implicated in disrupting MTs [9]. Hydrogen peroxide treatment depolymerizes and disorganizes MTs in human osteosarcoma 143B cells, rat pheochromocytoma PC-12 cells, AR42J pancreatic epithelial cells, and human umbilical cord vein endothelial HUVEC cells [10-13]. In addition, oxidative stress has been implicated in inducing MT disassembly in the setting of lung injury, resulting in pulmonary endothelial cell barrier dysfunction and increased inflammatory response [14]. EB proteins are also disrupted during oxidative stress. Le Grand *et al* [15] found that EB1 associates with MTs in a phosphorylation-dependent manner, which is affected by ROS. Smyth *et al* [16] found that EB1 is displaced from MTs in oxidative stress, correlating with decreased surface connexin 43 expression in human and mouse cardiomyocytes. Lastly, Cartelli *et al* [17] showed that increased ROS production caused reversals of EB3 comets and growth cone collapse in PC-12 cells.

Myocardial infarction (MI) occurs when a vascular occlusion reduces coronary blood flow, resulting in ischemia and necrosis [18]. The prolonged hypoxia can lead to formation of free radicals and oxidative stress in cardiomyocytes [19]. Post-infarction, myocytes can lose their structure and display abnormal protein expression, which could be a result of MT disruption [20, 21]. It has also been shown that tubulin levels are increased in hypertrophied and failing myocardium [22, 23]. Finally, MT content is increased in pressure-overload cardiac hypertrophy, lending support to the idea that compensatory increases in MT density enhances the rigidity of ventricular myocytes in heart failure [24, 25]. However, because these studies examined MT structure in fixed myocytes or used *in vitro* biochemical approaches, it is not known how MT dynamics change after MI, if oxidative stress might be implicated in these changes, and if these changes would have measurable physiological effects in the cell.

A set of key proteins, whose traffic to the membrane from the Golgi apparatus has been linked to MT movement, is the voltage-gated K_V4 channels. $K_V4.2$ and $K_V4.3$ are the pore-forming subunits responsible for the transient outward K^+ current (I_{to}). There is evidence that $K_V4.2$ and $K_V4.3$ are trafficked to the membrane via kinesin-17 and that interrupting dynein function can also alter expression of these channels [26, 27]. Previous research has shown that I_{to} is markedly reduced after MI and in hypertrophied hearts, leading to changes in action potential waveform in failing cardiomyocytes [28, 29]. At present, however, it is unclear if alterations in MTs during MI are implicated in the change in $K_V4.2$ and $K_V4.3$ expression seen after MI.

In this report, we take a direct approach to MT cardiac physiology. Confocal imaging showed that EB1 was localized on the Z-lines as well as along the length of MTs. Furthermore, using super-resolution nanoscopy, we found that the protein EB1 expresses along MTs in a punctate pattern. We quantified MT dynamics and found that MT growth was temperature dependent. Interestingly, most MTs assembled from one end of the sarcomere to the other. Under control conditions MT catastrophe rate was low and occurred mostly near the M-line. We found that MT dynamics are severely disrupted in MI, and that this disruption is due to the increase in oxidative stress in the cellular environment. Furthermore, we find that this disruption on MT physiology results in I_{to} and $K_V4.2$ and $K_V4.3$ density reduction, thus increasing action potential length after infarction.

2. Materials and Methods

2.1. Isolation of mouse ventricular myocytes

Mice were euthanized with a lethal dose of sodium pentobarbital administered intraperitoneally as approved by the University of Washington Institutional Animal Care and Use Committee. Ventricular myocytes were isolated using a Langendorff perfusion apparatus as previously described [30]. The isolated ventricular myocytes were kept either at room temperature (22 °C) or at 37 °C in Tyrode's solution containing (mM): 140 NaCl, 5 KCl, 10 HEPES, 10 glucose, 2 $CaCl_2$, and 1 $MgCl_2$; pH = 7.4 with NaOH, and used 0.5–8 h after isolation.

2.2. Myocardial infarction

The myocardial infarction model was produced as described previously [31]. Briefly, mice were anesthetized by isoflurane and non-invasively intubated. A left lateral thoracotomy was performed to expose the heart and the associated vasculature. The left ascending coronary artery was permanently ligated with a silk ligature and the thoracotomy was then closed. The infarct was obvious upon gross examination and myocytes were isolated from the left ventricle 48-72 h after the procedure.

2.3. Real Time qRT-PCR

For this study, EB1 and EB3 mRNA was quantified using real time quantitative RT-PCR as previously described [32, 33]. Total RNA was purified from mouse left ventricle, brain, or isolated cardiomyocytes using TRIzol reagent (Invitrogen, Waltham, MA) and RNeasy Mini Kit (Qiagen). The RNA was reverse transcribed using Super Script III First-Strand Synthesis

System (Invitrogen). qPCR was used to confirm the expression of EB1 and EB3. EB1 and EB3 qPCR primers were ordered from Qiagen (EB1 Cat. No. QT01169189, EB3 Cat. No. QT00168224) and compared using GAPDH (QT01658692) as a reference. The same procedure was used with tubulin (QT01060311), Kif2a (QT00174993), Katna1 (QT00107296), Kif18b (QT00115178), and Kif2c (Cat. No. QT00148708) to determine expression levels in the left ventricle and in isolated cardiomyocytes after infarction using GAPDH (QT01658692) as a reference.

2.4. Viral expression system

Adeno-associated virus serotype 9 (AAV9) expressing EB3-EGFP was generated by Vector Biolabs. Mice were anesthetized by isoflurane and injected retro-orbitally with AAV9 encoding the protein EB3 tagged with EGFP (AAV9-EB3-EGFP) [34, 35]. To allow expression of the protein, experiments were performed at least 3 weeks after virus injection.

2.5. Immunocytochemistry and imaging

Ventricular myocytes were imaged using an Olympus FluoView 1000 confocal microscope equipped with an Olympus 60× (NA = 1.49) oil immersion lens [30]. Super-resolution imaging was performed as described previously [36, 37]. Briefly, cardiomyocytes were fixed by incubating in 4% paraformaldehyde in PBS at 37 °C for 30 m, then washed with PBS and blocked for 1 h at room temperature in 50% SEA BLOCK (Thermo Fisher Scientific Waltham, MA) and 0.5% w/v Triton X-100 in PBS (blocking buffer). MTs were probed with a rat (Harlan, Indianapolis, IN, MAS 077) or mouse (Sigma, St. Louis, MO, T-9026) anti-tubulin antibody and mouse anti-EB1 antibody (BD transduction, San Jose, CA, 610534) or rat anti-EB3 antibody (Abcam, Cambridge, UK, ab53360) diluted to 1 μg/mL in blocking buffer by incubating overnight at 4 °C. Cells were washed extensively with 20% Sea Block three times. Cells were then incubated for 1 h at room temperature with donkey anti-rat Alexa Fluor 647 and goat anti-mouse Alexa Fluor 568 in blocking buffer. Myocytes were washed with 20% Sea Block three times and then mounted for imaging.

For immunocytochemistry, cells were mounted with PBS and sealed with nail polish. For super-resolution, the cells were mounted with imaging buffer containing: MEA-GLOX (MEA is cysteamine, GLOX is 0.56 mg/mL glucose oxidase, 34 μg/mL catalase, 10% w/v glucose), TN buffer (50 mM Tris pH 8.0, 10 mM NaCl). Slides were sealed with Twinsil (Picodent, Wiperfürth, Germany) sealant.

GSD super-resolution images of MTs and EB1 in fixed ventricular myocytes were generated with a Leica SR GSD 3D system consisting of a Leica DMI6000 B TIRF microscope equipped with a Leica oil-immersion HC PL APO 160x (NA = 1.43) objective, four laser lines (405 nm/30 mW, 488 nm/300 mW, 532 nm/500mW, and 642 nm/600mW), and an Andor iXon3 EM-OCD. Images were collected in TIRF mode with a 100 Hz frame rate for 20,000-100,000 frames using Leica Application Suite (LAS AF) software.

2.6. Fluorescent indicators

Some myocytes were loaded with 10 μM di8-ANEPPS (ThermoFisher) to label the location of T-tubules. In other experiments, myocytes were exposed to various concentrations of hydrogen peroxide (H_2O_2) while being imaged for EB3-EGFP movement or incubated for Western Blot protein expression experiments. To quantify oxidative stress, myocytes were loaded with 5 μM MitoSox-Red (ThermoFisher), a fluorescent indicator that localizes to the mitochondria and increases in fluorescence in response to oxidative species (e.g., superoxide, H_2O_2). We excited the indicator at 510 nm to yield a uniform signal assaying intracellular ROS [38, 39].

2.7. Image analysis

Colocalization was analyzed using the ImageJ plugin “JaCoP” after being after applying a threshold to eliminate noise. MT diameter data was generated on Image J by drawing a line perpendicular to the MT signal in an area where there was clear background signal on both sides and measuring the width of the signal. Each MT was measured 5 times and averaged to give an accurate measurement.

Each cell was scanned in the z-axis and recorded at a plane where the predominant number of MTs could be seen and tracked, usually in the midsection of the cell. MTs were tracked manually by generating a kymograph for each MT with strict parameters. For readers not familiar with this, kymographs can be conceptualized as an x-t scan, where the intensity along a given line is plotted for all images of a stack. We constructed kymographs by tracing the path of an MT throughout the image stack to form the x-axis of the kymograph image. The lines are then stacked along the y-axis for all frames in the image stack. In this paradigm, a growing MT will appear as a line oriented downward and to the right and a shrinking MT will appear as a line oriented downward and to the left. A catastrophe would be seen as a left facing angle (>) and a rescue is seen as a right facing angle (<). A pause is visualized as a vertical line.

Growth and shrinkage were evaluated only in linear circumstances ($R^2 < 0.85$ in linear regression analysis) as seen in many other studies [40-42]. MT pause was characterized by a MT tip moving less than 0.5 μm in 30 s [43]. Catastrophe and rescue were counted if: (1) they persisted for more than 15 s; (2) clear growth, shrinkage, or pause could be seen surrounding the event; and (3) movement exceeded that of pausing conditions. MTs were analyzed blind to experimental condition via name randomization [44, 45]. EB3-monitored dynamics was measured by counting the number of EB3-marked MTs in a given cell area, corrected for photobleaching using the Histogram Matching feature of Photocorrection in ImageJ [46].

2.8. Immunoprecipitation Western blotting

Protein expression for Kif2c was determined by Western blot, performed as previously described [47]. Briefly, proteins were extracted from control and MI mice left ventricle or cardiomyocytes and run on SDS-PAGE. To check Kif2c expression in cardiomyocytes, we immunoprecipitated Kif2c with Kif2c antibody in order to maximize possibility of seeing a band as the initial Western blot did not reveal protein expression. IgG was used as a negative control and testis tissue was used as a positive control. Cardiomyocyte protein lysates were incubated with anti-Kif2c antibody at 4°C for 2 hours and protein-antibody complexes were precipitated with protein-A/G-coupled agarose beads (Santa Cruz Biotech, Dallas, TX) at

4°C for overnight. The agarose beads were washed 4 times with IP-buffer and proteins were eluted by incubation at 100°C for 10 min in 2 × Laemmli sample buffer (Bio-Rad, Hercules, CA) supplemented with 5% 2-mercaptoethanol. The supernatants were then run on SDS-PAGE and proteins were transferred to PVDF membranes. After blocking with 5% normal donkey serum (Jackson ImmunoResearch, West Grove, PA), membranes were probed with anti-Kif2c primary antibody (Novus Biologicals, Littleton, CO, cat# NB100-2588) at room temperature for 2 h, followed by incubation with donkey anti-rabbit IgG alkaline phosphatase conjugated secondary antibody (Jackson ImmunoResearch) at room temperature for 1 h. The blots were developed with ECF (Amersham Biosciences, Piscataway, NJ) and imaged with Bio-Rad ChemiDoc XRS+ system.

2.9. Electrophysiology

Cells were kept at 37 °C during the day of the experiment. All electrophysiological recordings were performed while cells were superfused with saline solutions ≈37 °C. Pipettes were pulled using a Flaming-Brown type puller (Sutter Instruments, Novato, CA) with nominal resistance of 1-2 MΩ and filled with solutions as described below.

To record $I_{to,}$ membrane potential was controlled via the patch-clamp technique using an Axopatch 200B amplifier (Molecular Devices, Sunnyvale, CA). Data were acquired at 10 kHz and low-pass filtered at 2 kHz. Myocytes were perfused with Tyrode's solution while patched. After a GΩ seal was formed, a small amount of negative pressure was applied through the pipette to break the membrane and achieve a whole cell configuration. Once whole-cell configuration was successfully established in myocytes perfused with Tyrode's solution, the extracellular solution was exchanged for one with the following constituents (mM): 140 N-methyl-D-glucamine, 5.5 KCl, 10 HEPES, 0.1 CaCl2, 2 MgCl2, and 10 glucose; pH 7.4 with HCl. The pipette solution used in these experiments contained (mM): 110 K-aspartate, 30 KCl, 10 HEPES, 5 EGTA, and 4 Mg-ATP; pH 7.3. Cells were dialyzed with this solution. After a 100ms step to −50 mV to inactivate voltage-gated Na^+ channels, I_{to} was evoked by 2 s long depolarization pulses from −70 mV to potentials ranging from −70 to +80 mV (10 mV increment).

2.10. Surface biotinylation

Surface biotinylation was performed using a protocol adapted from Huang *et al* [48]. Briefly, cells were incubated with external control, colchicine, or H_2O_2 treatment for 4 h. After treatment, cells were exposed to 1 mg/mL of EZ-link sulfo-NHS-LC-LC-biotin (ThermoScientific) and incubated at room temperature for 30 m. Cells were washed with PBS + 100 mM glycine three times, then lysed using CHAPS lysis & IP buffer (FIVEphoton Biochemicals, San Diego, CA) with protease (Roche, Risch-Rotkreuz, Switzerland), sonicated, and centrifuged at 4 °C for 10 min. Total protein concentrations were determined and normalized between samples. Supernatant was mixed with immobilized Neutravidin beads (ThermoScientific) and rotated at 4 °C overnight. Beads were washed with 4 °C PBS 3 times and then combined with 2× Laemmli sample loading buffer (Bio-Rad) supplemented with 5% 2-mercaptoethanol. Beads were incubated for 10 m at 65 °C to elute proteins. Eluted proteins were then run on a 4-15% TGX precast gradient gel (Bio-Rad) and then electrophoresed proteins were transferred to a PVDF membrane. The membrane was blocked with 10% skim milk in TBST, then stained with $K_V4.2$ & $K_V4.3$ anti-rabbit primary antibody (Santa Cruz, Cat. No. sc-28634) in TBST with 1% BSA followed by goat anti-rabbit secondary antibody (Santa Cruz, Cat. No. sc-2057) in 5% skim milk in TBST before exposure.

2.11. Statistics

Data are presented as mean ± standard error of the mean (S.E.M.). Two-sample comparisons were made using a Student's *t* test ($^*P < 0.05$, $^{**}0.001 < P \le 0.01$, $^{**}P \le 0.001$).

3. Results

3.1. EB1 and tubulin co-localize in cardiomyocytes

We began our study by determining the level of expression of EB1 and EB3 transcript in ventricular myocytes using quantitative real time PCR (qRT-PCR). This analysis revealed that both of these genes were expressed in ventricular myocytes using GAPDH as a standard. However, EB1 was expressed to a larger extent than EB3 in heart. Expression in brain tissue was used for comparison (Figure 1A-B). These data suggest that EB1 is the predominant MT plus end binding protein in heart.

Thus, we investigated the spatial distribution of EB1 in ventricular myocytes using confocal and super-resolution microscopy. Figure 1C shows a confocal image of a ventricular myocyte labeled with EB1 (green) and tubulin-specific antibodies. Tubulin-associated fluorescence was located in tubules in the cytosol of the cell. Most MTs ran along the longitudinal axis of the cell. Figure 1D shows periodicity to the EB1 signal at intervals of ≈ 2 μm, suggesting a relationship to the Z-lines. We determined the Pearson's coefficient of EB1 and tubulin fluorescence signals (the merged image in Figure 1C) to provide a quantitative analysis of the degree of overlap between these two proteins. The Pearson co-efficient ranges from 0 (for non co-localized) to 1 (for fully co-localized) fluorescent signals. Indeed, we found that the Pearson's coefficient between EB1 and tubulin was 0.8 ± 0.1 (n = 5), indicating that at the level of resolution of our confocal microscope (~250 nm) these two proteins have a high degree of co-localization in ventricular myocytes, as most EB1 can be found along the length of the MTs.

We used ground state depletion (GSD) nanoscopy of EB1 and tubulin to obtain higher resolution maps of the localization of these proteins in ventricular myocytes. The resolution of the super-resolution GSD microscope is ~30 nm. Figure 1E shows a representative super-resolution localization map of tubulin (red) and EB1 (green) in a section of a ventricular myocyte. The inset shows the full image as well as the location of the zoomed in region. We detected a punctate pattern of EB1 localization along the MT lattice. We saw a similar expression profile and co-localization with tubulin when imaging endogenous EB3 using our super-resolution system (Figure S1). The diameter of these MTs was 42.0 ± 2.8 nm (n = 9). We calculate that our primary and secondary antibody staining system on average adds about 17 nm to our measurements, which means that we imaged MTs to be ~25 nm thick, which is consistent with the literature [49].

3.2. Live imaging of MTs in ventricular myocytes

Having shown that EB1 is expressed in small puncta along MTs in ventricular myocytes, we investigated MT dynamics in these cells. Although EB1 is more prevalent in the heart and better for native protein fixed cell imaging, we chose to use EB3 for our viral vector expression system because it is functionally similar to EB1 and because it is widely regarded to be superior in live imaging studies [50].

We generated an AAV9-EB3-EGFP viral vector and injected it retro-orbitally into live mice, allowing sufficient time for the virus to infect live ventricular myocytes before isolating cells. In addition to labeling the MT ends and lattice, we also saw the presence of bands oriented transversely along the cell (Figure 2A). These bands were periodic in nature at ≈ 2 μm apart. In order to determine their relation to the sarcomere, we stained myocytes with di8-ANNEPPS, a marker of T-tubules. The di8-ANEPPS signal and EB3-EGFP bands co-localize perfectly, showing that cytoplasmically expressed EB3 also localizes to the T-tubules/Z-lines.

In addition to being localized to the T-tubules/Z-lines, the EB3-EGFP protein also labeled MT ends, enabling us to image MTs in acutely dissociated adult ventricular myocytes. We used these data to analyze MT tip translocation, and thus MT dynamics, by recording 2D images of the cell at a frequency of 1 frame every ≈ 5-10 s and creating kymographs. Kymographs like the ones shown in Figure 2B were generated from the image stack (Figure 2A).

Figure 2B shows two kymographs from a representative myocyte showing MT growth at 22 (top) and physiological 37 °C (bottom). Labels show areas of growth, shrinkage, pause, rescue, and catastrophe. At 22 °C, this MT grew at a rate that ranged from 0.01-0.02 $\mu m{*}s^{-1}$. There was one rescue event in this MT kymograph. The MT we recorded at 37 °C had a much higher rate of growth (0.08 $\mu m{*}s^{-1}$) than the one recorded at 22 °C.

We used analysis from several kymographs generated from images of MTs growing at 22 °C to quantify multiple MT dynamics: growth rate and distance, shrinkage rate and distance, catastrophe rate, and rescue rate (Figure 2C-E; Movie 1). While dynamic MTs could be scored at 22 °C, at physiological 37 °C, MTs were much more dynamic. MT growth rate and shrink rate were greatly increased, as was growth distance and shrink distance. Lastly, catastrophe rate rescue rate were also increased. These data show that, in every parameter, the dynamicity of MTs was significantly increased between room temperature and physiological temperature (Figure 2C-E; Movie 2).

We quantified the directionality of MT growth at physiological temperature (Figure 2F). The vast majority (~80%) of all MTs grew along the horizontal axis of the cardiomyocytes, traversing between T-tubules. We calculated the ratio between leftward growing and rightward growing horizontal MTs to be 0.97 ± 0.05 (n = 176), indicating that MT polarity was evenly mixed relative to the horizontal axis of the cell. Thirteen percent of MTs grew diagonally, usually around nuclei. A small fraction of MTs (7%) grew vertically, almost always along the Z-line, both upward and downward. In addition, 91% of the time that a MT paused, that is, rested between two growth periods or shrink periods, it was on a Z-line, suggesting that the Z-line provides some mechanism of stability for the MT. Lastly, 82% of MTs were confined to a single sarcomere for the duration of our recordings (at least 10 min). 14% of MTs spanned 2 sarcomeres, 2.4% spanned 3 sarcomeres, and 1.7% spanned over 3 sarcomeres.

We also applied 1 μM colchicine, a MT depolymerizer, to the myocytes (Figure 2G, Movie 3). As expected, the MTs underwent catastrophe and depolymerized. After ten minutes, a significant loss in EB3-monitored dynamics was observed, thus showing in real time the use of colchicine as an artificial inducer of MT catastrophe and depolymerization (Figure 2H). Lastly, we were able to compare MTs in ventricular myocytes to those in other cells by transfecting EB3-EGFP into human embryonic (tSA-201) cells and assaying dynamics. We found no significant difference between MT growth and shrinkage rates in either cell model ($p > 0.05$).

3.3. Oxidative stress disrupts MT dynamics

Next, we tested the hypothesis that oxidative stress disrupts MT dynamics. To do this, we recorded EB3-EGFP images before and after application of 200 μM H_2O_2, an inducer of oxidative stress at a concentration known to induce injury in ventricular myocytes [51]. The myocytes used in these experiments were loaded with MitoSox Red, a mitochondrial-targeted indicator that increases in fluorescence intensity based on the amount of ROS (e.g., super oxide and H_2O_2) present in a given cell (Figure 3, Movie 4). Figure 3A shows an examplary cell with EB3-EGFP in green and the MitoSox Red signal in red inset. Superfusion with an external solution containing 200 μM H_2O_2 progressively increased the MitoSox Red signal, showing an increase in cell oxidative stress, and also altered MT dynamics. On average ($n = 5$), the MitoSox Red signal's change in fluorescence upon application of 200 μM H_2O_2 shows that the cell's level of oxidative stress increases in a seemingly sigmoidal fashion that plateaus around 10 minutes, reaching a level of ≈ 3 F/F_0 (Figure 3B). Over the course of these 10 minutes, similar to colchicine, we saw MTs undergo catastrophe and depolymerize.

Figure 3C shows five example kymographs of MTs from the cell shown in Figure 3A. In each kymograph, the MTs grow, and then undergo a period of dynamic instability and catastrophe before depolymerizing. In most cases (kymographs 1-4), the MT depolymerizes soon after application of 200 μM H_2O_2. The period of instability is also variable, lasting anywhere from less than a minute (kymograph 5) to over 7 minutes (kymograph 4). Through this time course, EB3-monitored dynamics decreased and became completely absent after 10 minutes of 200 μM H_2O_2 application in a similar fashion to that seen upon colchicine application (Figure 3D).

3.4. Live imaging of MTs in ventricular myocytes post-MI

Because oxidative stress increases following MI [19], we tested the hypothesis that MI would alter MT dynamics. We performed total left ascending coronary occlusion in mice injected with AAV9-EB3-EGFP to mimic MI and isolated cardiomyocytes 48-72 hours later (Figure 4, Movie 5). Similar to application of 200 μM H_2O_2, MT dynamics were significantly altered. Figure 4A shows kymographs of a MT imaged in a control vs. infarcted mouse. In this MI sample kymograph, there were 3 catastrophic events and 3 rescue events.

Taking an ensemble of MT kymographs from MI mice shows that while growth rate, growth distance, and shrink distance were unchanged between control and infarcted mice, shrinkage rate, catastrophe rate, and rescue rate were significantly higher (Figure 4B-D). Figure 4E shows a quantification of catastrophe and rescue in regards to the position of the head of the MT on the Z-line by cell. In every cell, there were more catastrophic events when the head of the MT was between rather than on a Z-line and more rescue events when the head of the MT was on rather than between Z-lines. Overall, 68% of catastrophic events occurred between Z-lines and 84% of rescue events occurred on Z-lines.

We explored possible explanations for the increase in catastrophic events seen after MI (Figure S2). A quantitative real time qRT-PCR screen of molecular inducers of catastrophe between control vs. infarcted cells revealed no change in RNA expression for Kif2a, Katna1, or Kif18b relative to GAPDH [52-54]. There was a non-significant trend towards increased tubulin expression ($p < 0.08$). There was a significant increase in Kif2c protein expression (Figure S2A) [55]. However, on Western blot, there was no band seen in either control or infarcted cells (data not shown). We also performed a co-IP blot using Kif2c to try and use a more sensitive technique to assay protein expression, which showed a prominent band when using the entire left ventricle after MI but no band with isolated cardiomyocytes (Figure S2B). In addition, we were unable to visualize Kif2c with antibody-mediated imaging on control or infarcted cells. Kif2c has only been reported to be associated with dividing cells and has never been found in terminally differentiated cardiac tissue. Furthermore, Kif2C expression is lost from postmitotic C2C12 cells as they undergo myofibrillogenesis [56]. Thus, we conclude that the increase seen in Kif2c transcript after MI is likely due to fibroblasts and other dividing cells migrating into the infarcted region rather than novel expression of this molecular inducer of catastrophe in ventricular myocytes.

3.5. Oxidative stress mimics MT dynamic disruptions seen after MI

After discovering and quantifying MT dynamic disruptions in our model of MI, we tested the hypothesis that oxidative stress was responsible for this change in MT dynamics. Using myocytes loaded with MitoSox Red and solutions with varied H_2O_2 concentrations, we performed a concentration response curve to assay the effect of H_2O_2 on cell oxidative stress. We found that MitoSox Red fluorescence increased linearly over the range of H_2O_2 concentrations (0-100 μM) used in these experiments (Figure 5A). We measured the average fluorescence of MitoSox Red in MI cardiomyocytes and found that the amount of oxidative stress was equivalent to application of about 10-20 μM H_2O_2 to control (i.e., non-MI) myocytes.

Many of the cells died or became unhealthy after prolonged (>30 min) exposure to 20 μM H_2O_2, so we assayed and quantified MT dynamics at 10 μM H_2O_2 (Figure 5, Movie 6). Figure 5B shows a kymograph of a MT from a cell exposed to 10 μM H_2O_2, with 4 catastrophic events and 4 rescues present. We found that growth rate, growth distance, and shrink distance were similar to control cells. However, like infarcted cells, the shrink rate, catastrophe rate, and rescue rate were significantly different from control ventricular myocytes (Figure 5C-E). From these data, we conclude that 10 μM H_2O_2 application, which induces the level of oxidative stress within the range seen in our MI model, is also able to replicate the disruptions in MT dynamics seen during this pathological condition.

3.6. MT dynamic disruptions reduce I_{to} density

Lastly, we tested the impact of MT dynamics on ventricular myocyte physiology by testing the hypothesis that changes in MT dynamics would inhibit trafficking of ion channels, namely $K_V4.2$ and $K_V4.3$, to the membrane. We quantified I_{to} density as well as $K_V4.2$ and $K_V4.3$ surface expression in control and MI cells (Figure 6). We found that I_{to} density was significantly reduced in MI cells at all positive voltages (Figure 6A-B). Application of 10 μM H_2O_2 to control cells recapitulated the decrease in I_{to} density seen in MI, as did application of 1 μM colchicine. Co-application of H_2O_2 and colchicine did not further reduce I_{to}, lending support to the argument that both reagents are working by the same mechanism of MT polymer loss and that H_2O_2 application is not causing a decrease in I_{to} by other mechanisms. Using surface biotinylation binding with Western blot, we assayed surface expression of $K_V4.2$ and $K_V4.3$ in control and MI ventricular myocytes as well as after application of 10 μM H_2O_2 and application of 1 μM colchicine (Figure 6C). After isolation, cells were incubated for 4 hours to allow time for MT trafficking defects to be seen. By quantifying the amount of protein bound to biotin in ratio to the amount of total protein found in the cell lysis, we found that surface expression of $K_V4.2$ and $K_V4.3$ was significantly decreased in infarcted cells as well as after application of H_2O_2 and colchicine. This is consistent with the view that the reduction in I_{to} seen was due to defects in $K_V4.2$ and $K_V4.3$ trafficking rather than any other mechanism.

4. Discussion

In this study, we were able to visualize dynamic MTs in living, acutely dissociated ventricular myocytes and made fundamental observations regarding these cytoskeletal structures. Our data suggest that EB proteins accumulate in bands at or near the Z-lines/T-tubules that run perpendicular to the longitudinal axis of ventricular myocytes. MTs are highly dynamic, growing, and shrinking within ventricular myocytes. MTs grow from Z-line-to-Z-line in ventricular myocytes and appear to be stabilized at the Z line, as evidenced by decreased catastrophe rate, increased rescue rate, and the prevalence of pausing. Finally, we found that increased oxidative stress during MI increases the catastrophe rate of MTs, decreasing I_{to} in ventricular myocytes. The physiological implications of these findings are discussed below.

Super-resolution and confocal imaging revealed EB1 punctate localization along the MT lattice. Interestingly, we also found that EB1 and transfected EB3 accumulated in the Z-lines of ventricular myocytes, which is where most MTs start growing. Although the molecular mechanisms causing EB1 and EB3 expression in the Z-line are unclear, protein-protein interaction may be important here. For example, it is possible that EB proteins link with proteins on the Z-line for MT stability, cargo transfer, or other cellular processes. Future studies should investigate these issues in detail.

A recent study by Oddoux *et al* [57] imaged MTs in live skeletal muscle cells using super resolution STED microscopy. Similar to our findings, they found that EB3-GFP was localized not only to the tips, but also along the entirety of the MT and that puncta moved mostly longitudinally or transversely with no regard to cell polarity at similar growth rates. Furthermore, EB3 movement was localized to Z-lines of skeletal muscle. Interestingly, their data indicate that MTs are most likely forming a dynamic lattice and that they grow over each other in bundles. Furthermore, Oddoux *et al* [57] speculates that dystrophin may serve to guide and define regions of MT growth and propose that MT pathology may be implicated in muscular dystrophy. Similarly, Belanto *et al* showed that dystophin is capable of pausing MTs in vitro [58]. As ROS is also implicated in several muscular dystrophies, these studies appear to be synergistic. In combination, our data and that of Oddoux *et al* [57], suggest that MTs in striated muscle (i.e., cardiac and skeletal) have similar structural and dynamic properties.

MTs in ventricular myocytes grow at a rate of ≈0.07 microns per second at physiological temperatures. This means that a MT could move from one Z-line to another in about 30 seconds, assuming it does not pause. Considering that most molecular motors translocate along MT lattice faster, for example, kinesin 1 and dynein both process at a rate of ≈ 1 $\mu m*s^{-1}$ depending on their load, MT growth would be the limiting factor in organelle and protein transport in ventricular myocytes [59]. Interestingly, the direction of MT growth did not appear to be random, as the vast majority of the time MTs grew from Z-line-to-Z-line without preference to cell polarity. This is distinctly different from non-muscle cells, where MTs grow in multiple directions [60]. Indeed, the average growth distance we observed in ventricular myocytes was about 2 μm, roughly the distance between Z-lines.

Related to this, Hong *et al* [61] have supplied evidence that bridging indicator protein 1 (BIN1), the protein which localizes $Ca_V1.2$ to the surface membrane and induces formation of T-tubules, also stabilizes MTs. It is possible that MTs may be involved in transporting proteins to the dyad for use in excitation-contraction coupling, moving horizontally from dyad to dyad to optimize each dyad for Ca^{2+} signaling. More work needs to be done to determine why T-tubules seem to stabilize MTs, and what physiological roles this stabilization plays in excitation-contraction coupling. Nevertheless, our data suggests that if MTs are involved in trafficking proteins to and from the T-tubule and SR dyad, then rapid changes in MT dynamics could alter the protein composition in these compartments in a matter of minutes.

Our data, in combination with the findings of a recent study, provide insights into the molecular mechanisms underlying increased MT catastrophe in ventricular myocytes isolated from infarcted hearts. We, as others [19, 62, 63], found that oxidative stress increases after MI. Phosphorylation of EB1 by the glycogen synthase kinase 3β (GSK3β) increases binding of EB1 to the MT plus tip [15]. ROS inhibits GSK3β and EB1 accumulation in the MT plus end. Together, these findings suggest that higher oxidative stress after MI inhibits GSK3β, which decreases EB phosphorylation and thus promotes EB dislocation from the MTs, which destabilizes these cytoskeletal structures.

The increase in catastrophes seen after MI has significant implications for ventricular myocyte physiology. As our data suggest, it strongly correlates with decreases in $K_V4.2$ and $K_V4.3$ channels in the membrane and thus decreases I_{to} density after MI. K_V channels may not be the only K+ channels regulated by MT dynamics, however. The mechanism linking increased MT catastrophe to decreased K_V currents likely involves the disruption of the "tracks" by which vesicles containing these channels are transported by kinesin-17 and dynein to and from the membrane [27, 64]. Recently, Arakel *et al* [65] showed that ATP-sensitive K^+ channels (K_{ATP}) are held at the Golgi and released under β-adrenergic stimulation in ventricular myocytes. As MTs are nucleated at the Golgi in striated muscle [57], it is intriguing to speculate that transport of vesicles containing K_{ATP} channels is activated by protein kinase A during β-adrenergic signaling, thereby increasing the incorporation of these channels into the sarcolemma of ventricular myocytes.

Our study investigated MT dynamics during acute MI, when most ventricular myocyte remodeling is electrophysiological. However, our findings suggest that increasing MT dynamics could also impact the long-term (i.e., >1 week) structural stability of these cells post-infarction. It is established that MI results in a loss of T-tubules [66-68]. If MTs are stabilized by BIN1 and thus by T-tubules, the loss of T-tubules would create areas in the cell where MTs would be unstable and unable to grow. These would represent areas of most severe injury. As a result, proteins might be trafficked preferentially to areas of the cell that are healthier, and thus this reorganization might facilitate cellular recovery. Indeed in our data, we saw areas where catastrophe seemed to be more prevalent after MI. On the other hand, many proteins would be unable to get to the surface membrane, resulting in a significant loss of resources and inefficiency for an injured cell. Restoring MT dynamics after MI, using pharmacology or other means, may help increase the surface expression of trafficked proteins and help stabilize cell physiology in the critical time period after infarction.

At present, the mechanism for directional (i.e., Z-line-to-Z-line) MT growth in heart is unclear. One possibility is that MTs are "forced" to grow in a specific direction due to structural constraints. In this model, MTs would be able to grow primarily between myosin-actin fibers within each sarcomere. These inter-fiber "tunnels" would provide access to growing MTs and their cargo for delivery. Furthermore, it raises the possibility that MTs also provide additional structural support to the sarcomere. Future studies, should examine this intriguing possibility.

All MT parameters we examined in ventricular myocytes were temperature-dependent: growth, shrink, catastrophe and rescue. This finding is relevant because most MT studies in ventricular myocytes have been traditionally performed at temperatures typically ranging from 21-23 °C. Our study suggests that drawing conclusions from MT-related processes from studies at these temperatures could be misleading. Increasing temperature to physiological levels resulted in a significant increase in MT dynamics. This finding is important for the entire cardiac electrophysiological field moving forward, as the vast majority of experiments are conducted at room temperature. If cardiomyocytes sit at room temperature throughout the experimental day, it is likely that their MTs are less dynamic, leading to changes in protein trafficking. Our data suggests that cardiomyocytes should be incubated at 37 °C after being isolated in order to approximate normal cell physiology.

Limitations of the study

All studies that investigate the effects of myocardial infarction and involve expression of endogenous proteins on a wild type background should be interpreted cautiously. For example, although endogenous EB1, EB3, and exogenous EB3-EGFP are expressed on the on the MTs as well as on the t-tubules/Z-lines of ventricular myocytes, expression of EB3-EGFP in these structures could be potentially higher than under control conditions. Furthermore, in our MI studies we did not segregate cells based on their proximity to the infarct zone. Thus, we likely recorded cells in various levels of injury. In spite of these limitations, we contend that novel insights into the bases of MT dynamics in ventricular myocytes have been obtained in the present experiments. These insights should form the bases of new hypotheses that can be best tested in appropriate animal models.

Summary and conclusions

To conclude, MTs have important roles in cardiomyocytes. By live-imaging MTs, we were able to assay their dynamics and provide valuable insights regarding how MTs move within cardiomyocytes. We also quantified how oxidative stress disrupts MTs in the setting of MI. We showed that this disruption in MTs has direct impacts on cell physiology, decreasing I_{to} by reducing $K_v4.2$ and $K_v4.3$ surface expression.

Supplementary Material

Refer to Web version on PubMed Central for supplementary material.

Acknowledgements

We thank Ms. Jennifer Cabarrus and Mr. Ken Bible for technical assistance, and the labs of Dr. Stanley Froehner and Dr. Chris Liu for providing laboratory equipment and space, especially Dr. Marv Adams. We thank Dr. Chip Asbury for helpful discussion, and Drs. Rosie Dixon and Ana De La Mata Sampedro for editing the manuscript. In addition, Dr. Claudia Moreno helped with image processing. This study was supported by NIH grants HL085686, GM069429, and F30 HL126249-02, the AHA Predoctoral Fellowship, as well as the ARCS Foundation.

References

1. Gelfand VI, Bershadsky AD. Microtubule dynamics: mechanism, regulation, and function. Annu Rev Cell Biol. 1991; 7:93–116. [PubMed: 1809357]
2. Kerfant BG, Vassort G, Gomez AM. Microtubule disruption by colchicine reversibly enhances calcium signaling in intact rat cardiac myocytes. Circ Res. 2001; 88:E59–65. [PubMed: 11304499]
3. Mitchison T, Kirschner M. Dynamic instability of microtubule growth. Nature. 1984; 312:237–42. [PubMed: 6504138]
4. Desai A, Mitchison TJ. Microtubule polymerization dynamics. Annual review of cell and developmental biology. 1997; 13:83–117.
5. Gu C, Zhou W, Puthenveedu MA, Xu M, Jan YN, Jan LY. The microtubule plus-end tracking protein EB1 is required for Kv1 voltage-gated K+ channel axonal targeting. Neuron. 2006; 52:803–16. [PubMed: 17145502]
6. Shaw RM, Fay AJ, Puthenveedu MA, von Zastrow M, Jan YN, Jan LY. Microtubule plus-end-tracking proteins target gap junctions directly from the cell interior to adherens junctions. Cell. 2007; 128:547–60. [PubMed: 17289573]

7. Akhmanova A, Steinmetz MO. Tracking the ends: a dynamic protein network controls the fate of microtubule tips. Nature reviews Molecular cell biology. 2008; 9:309–22. [PubMed: 18322465]
8. Zhang S, Shaw RM. Multilayered regulation of cardiac ion channels. Biochimica et biophysica acta. 2013; 1833:876–85. [PubMed: 23103513]
9. Parker AL, Kavallaris M, McCarroll JA. Microtubules and their role in cellular stress in cancer. Front Onco. 2014; 4:1–19.
10. Lee C, Liu C, Hsieh R, Wei Y. Oxidative Stress-Induced Depolymerization of Microtubules and Alteration of Mitochondrial Mass in Human Cells. Ann N Y Acad Sci. 2005; 1042:246–54. [PubMed: 15965069]
11. Valen G, Sonden A, Vaage J, Malm E, Kjellstrom BT. Hydrogen peroxide induces endothelial cell atypia and cytoskeleton depolymerization. Free radical biology & medicine. 1999; 26:1480–88. [PubMed: 10401612]
12. Hinshaw DB, Miller MT, Omann GM, Beals TF, Hyslop PA. A cellular model of oxidant-mediated neuronal injuty. Brain Res. 1993; 615:13–26. [PubMed: 8364721]
13. Hu W, Lu Q. Impact of oxidative stress on the cytoskeleton of pancreatic epithelial cells. Exp Ther Med. 2014; 8:1428–42. [PubMed: 25289034]
14. Kratzer E, Tian Y, Sarich N, Wu T, Meliton A, Leff A, et al. Oxidative stress contributes to lung injury and barrier dysfunction via microtubule destabilization. Am J Respir Cell Mol Biol. 2012; 47:688–97. [PubMed: 22842495]
15. Le Grand M, Rovini A, Bourgarel-Rey V, Honore S, Bastonero S, Braguer D, et al. ROS-mediated EB1 phosphorylation through Akt/GSK3beta pathway: implication in cancer cell response to microtubule-targeting agents. Oncotarget. 2014; 5:3408–23. [PubMed: 24930764]
16. Smyth JW, Hong TT, Gao D, Vogan JM, Jensen BC, Fong TS, et al. Limited forward trafficking of connexin 43 reduces cell-cell coupling in stressed human and mouse myocardium. J Clin Invest. 2010; 120:266–79. [PubMed: 20038810]
17. Cartelli D, Ronchi C, Maggioni MG, Rodighiero S, Giavini E, Cappelletti G. Microtubule dysfunction precedes transport impairment and mitochondria damage in MPP+-induced neurodegeneration. Journal of neurochemistry. 2010; 115:247–58. [PubMed: 20649848]
18. Diaz-Munoz M, Alvarez-Perez MA, Yanez L, Vidrio S, Martinez L, Rosas G, et al. Correlation between oxidative stress and alteration of intracellular calcium handling in isoproterenol-induced myocardial infarction. Molecular and cellular biochemistry. 2006; 289:125–36. [PubMed: 16820956]
19. Hori M, Nishida K. Oxidative stress and left ventricular remodelling after myocardial infarction. Cardiovascular research. 2009; 81:457–64. [PubMed: 19047340]
20. Heling A, Zimmermann R, Kostin S, Maeno Y, Hein S, Devaux B, et al. Increased expression of cytoskeletal, linkage, and extracellular proteins in failing human myocardium. Circ Res. 2000; 86:846–53. [PubMed: 10785506]
21. Iwai K, Hori M, Kitabatake A, Kurihara H, Uchida K, Inoue M, et al. Disruption of microtubules as an early sign of irreversible ischemic injury. Immunohistochemical study of in situ canine hearts. Circ Res. 1990; 67:694–706. [PubMed: 1697795]
22. Aquila-Pastir LA, DiPaola NR, Matteo RG, Smedira NG, McCarthy PM, Moravec CS. Quantitation and distribution of beta-tubulin in human cardiac myocytes. J Mol Cell Cardiol. 2002; 34:1513–23. [PubMed: 12431450]
23. Zhang C, Chen B, Guo A, Zhu Y, Miller JD, Gao S, et al. Microtubule-mediated defects in junctophilin-2 trafficking contribute to myocyte transverse-tubule remodeling and Ca2+ handling dysfunction in heart failure. Circulation. 2014; 129:1742–50. [PubMed: 24519927]
24. Tsutsui H, Ishihara K, Cooper Gt. Cytoskeletal role in the contractile dysfunction of hypertrophied myocardium. Science. 1993; 260:682–7. [PubMed: 8097594]
25. Tagawa H, Koide M, Sato H, Zile MR, Carabello BA, Cooper Gt. Cytoskeletal role in the transition from compensated to decompensated hypertrophy during adult canine left ventricular pressure overloading. Circ Res. 1998; 82:751–61. [PubMed: 9562434]
26. Loewen ME, Wang Z, Eldstrom J, Dehghani Zadeh A, Khurana A, Steele DF, et al. Shared requirement for dynein function and intact microtubule cytoskeleton for normal surface expression

of cardiac potassium channels. Am J Physiol Heart Circ Physiol. 2009; 296:H71–83. [PubMed: 18978193]

27. Chu PJ, Rivera JF, Arnold DB. A role for Kif17 in transport of Kv4.2. J Biol Chem. 2006; 281:365–73. [PubMed: 16257958]
28. Nabauer M, Beuckelmann DJ, Erdmann E. Characteristics of transient outward current in human ventricular myocytes from patients with terminal heart failure. Circ Res. 1993; 73:386–94. [PubMed: 8330381]
29. Wagner M, Goltz D, Stucke C, Schwoerer AP, Ehmke H, Volk T. Modulation of the transient outward K+ current by inhibition of endothelin-A receptors in normal and hypertrophied rat hearts. Pflugers Arch. 2007; 454:595–604. [PubMed: 17333248]
30. Drum BM, Dixon RE, Yuan C, Cheng EP, Santana LF. Cellular mechanisms of ventricular arrhythmias in a mouse model of Timothy syndrome (long QT syndrome 8). J Mol Cell Cardiol. 2014; 66:63–71. [PubMed: 24215710]
31. Kolk MV, Meyberg D, Deuse T, Tang-Quan KR, Robbins RC, Reichenspurner H, et al. LAD-ligation: a murine model of myocardial infarction. J Vis Exp. 2009
32. Amberg GC, Santana LF. Downregulation of the BK channel beta1 subunit in genetic hypertension. Circ Res. 2003; 93:965–71. [PubMed: 14551242]
33. Amberg GC, Bonev AD, Rossow CF, Nelson MT, Santana LF. Modulation of the molecular composition of large conductance, Ca^{2+} activated K^+ channels in vascular smooth muscle during hypertension. J Clin Invest. 2003; 112:717–24. [PubMed: 12952920]
34. Bish LT, Morine K, Sleeper MM, Sanmiguel J, Wu D, Gao G, et al. Adeno-Associated Virus (AAV) Serotype 9 Provides Global Cardiac Gene Transfer Superior to AAV1, AAV6, AAV7, and AAV8 in the Mouse and Rat. Hum Gene Ther. 2008; 19:1359–68. [PubMed: 18795839]
35. Inagaki K, Fuess S, Storm TA, Gibson GA, Mictiernan CF, Kay MA, et al. Robust Systemic Transduction with AAV9 Vectors in Mice: Efficient Global Cardiac Gene Transfer Superior to that of AAV8. Mol Ther. 2006; 14:45–53. [PubMed: 16713360]
36. Dixon RE, Moreno CM, Yuan C, Opitz-Araya X, Binder MD, Navedo MF, et al. Graded Ca^{2+}/calmodulin-dependent coupling of voltage-gated $Ca_V1.2$ channels. eLife. 2015:4.
37. Mercado J, Baylie R, Navedo MF, Yuan C, Scott JD, Nelson MT, et al. Local control of TRPV4 channels by AKAP150-targeted PKC in arterial smooth muscle. J Gen Physiol. 2014; 143:559–75. [PubMed: 24778429]
38. Zielonk J, Vasquez-Vivar J, Kalyanaraman B. Detection of 2-hydroxyethidium in cellular systems: a unique marker product of superoxide adn hydroethidine. Nat Protoc. 2008; 3:8–21. [PubMed: 18193017]
39. Kalyanaraman B, Darley-Usmar V, Davies KJA, Dennery PA, Forman HJ, Grisham MB, et al. Measuring reactive oxygen and nitrogen species with fluorescent probes: challenges and limitations. Free radical biology & medicine. 2012; 52:1–6. [PubMed: 22027063]
40. Tanaka K, Kitamura E, Kitamura Y, Tanaka TU. Molecular mechanisms of microtubule-dependent kinetochore transport toward spindle poles. J Cell Biol. 2007; 178:269–81. [PubMed: 17620411]
41. Kosco KA, Pearson CG, Maddox PS, Wang PJ, Adams IR, Salmon ED, et al. Control of Microtubule Dynamics by Stu2p Is Essential for Spindle Orientation and Metaphase Chromosome Alignment in Yeast. Mol Biol Cell. 2001; 12:2870–80. [PubMed: 11553724]
42. Tirnauer JS, O'Toole E, Berrueta L, Bierer BE, Pellman D. Yeast Bim1p Promotes the G1-specific Dynamics of Microtubules. J Cell Biol. 1999; 145:993–1007. [PubMed: 10352017]
43. Kline-Smith SL, Walczak CE. The microtubule-destabilizing kinesin XKCM1 regulates microtubule dynamic instability in cells. Mol Biol Cell. 2002; 13:2718–31. [PubMed: 12181341]
44. Labbe J, Maddox PS, Salmon ED, Goldstein B. PAR Proteins Regulate Microtubule Dynamicsat the Cell Cortex in C. elegans. Curr Biol. 2003; 13:707–14. [PubMed: 12725727]
45. Peris L, Wagenbach M, Lafanechere L, Brocard J, Moore AT, Kozielski F, et al. Motor-dependent microtubule disassembly driven by tubulin tyrosination. J Cell Biol. 2009; 185:1159–66. [PubMed: 19564401]
46. Montenegro Gouveia S, Leslie K, Lapitein LC, Buey RM, Grigoriev I, Wagenbach M, et al. In vitro reconstitution of the functional interplay between MCAK and EB3 at microtubule plus ends. Curr Biol. 2010; 20:1717–22. [PubMed: 20850319]

47. Cheng EP, Yuan C, Navedo MF, Dixon RE, Nieves-Cintron M, Scott JD, et al. Restoration of normal L-type Ca2+ channel function during Timothy syndrome by ablation of an anchoring protein. Circ Res. 2011; 109:255–61. [PubMed: 21700933]
48. Huang GN, Zeng W, Kim JY, Yuan JP, Han L, Muallem S, et al. STIM1 carboxyl-terminus activates native SOC, I(crac) and TRPC1 channels. Nat Cell Biol. 2006; 8:1003–10. [PubMed: 16906149]
49. Vaughan JC, Jia S, Zhuang X. Ultrabright photoactivatable fluorophores created by reductive caging. Nat Methods. 2012; 9:1181–4. [PubMed: 23103881]
50. Sironi L, Solon J, Conrad C, Mayer T, Brunner D, Ellenberg J. Automatic Quantification of Microtubule Dynamics Enables RNAi-screening of New Mitotic Spindle Regulators. Cytoskeleton. 2011; 68:266–78. [PubMed: 21491614]
51. Xie J, Zhou X, Hu X, Jiang H. H2O2 Evokes Injury of Cardiomyocytes Through Upregulating HMGB1. Hellenic J Cardiol. 2013; 54:101–6.
52. Ganem NJ, Compton DA. The KinI kinesin Kif2a is required for bipolar spindle assembly through a functional relationship with MCAK. J Cell Biol. 2004; 166:473–8. [PubMed: 15302853]
53. Zhang D, Grode KD, Stewman S, Diaz D, Liebling E, Rath U, et al. Drosophila Katanin is a microtubule depolymerase that regulates cortical-microtubule plus-end interactions and cell migration. Nat Cell Biol. 2011; 13:361–70. [PubMed: 21378981]
54. Stout JR, Yount AL, Powers JA, LeBlanc C, Ems-McClung SC, Walczak CE. Kif18B interacts with EB1 and controls astral microtubule length during mitosis. Mol Biol Cell. 2011; 22:3070–80. [PubMed: 21737685]
55. Newton CN, Wagenbach M, Ovechkina Y, Wordeman L, Wilson L. MCAK, a Kin I kinesin, increases the catastrophe frequency of steady-state HeLa cell microtubules in an ATP-dependent manner in vitro. FEBS Lett. 2004; 573:80–4. [PubMed: 15304328]
56. Ginkel LM, Wordeman L. Expression and partial characterization of kinesin-related proteins in differentiating and adult skeletal muscle. Mol Biol Cell. 2000; 11:4143–58. [PubMed: 11102514]
57. Oddoux S, Zaal KJ, Tate V, Kenea A, Nandkeolyar SA, Reid E, et al. Microtubules that form the stationary lattice of muscle fibers are dynamic and nucleated at Golgi elements. J Cell Biol. 2013; 203:205–13. [PubMed: 24145165]
58. Belanto JJ, Mader TL, Eckhoff MD, Strandjord DM, Banks GB, Gardner MK, et al. Microtubule binding distinguishes dystrophin from utrophin. Proc Natl Acad Sci U S A. 2014; 111:5723–8. [PubMed: 24706788]
59. Muller MJI, Klumpp S, Lipowsky R. Motility states of a molecular motors engaged in a stochastic tug-of-war. J Stat Phys. 2008; 133:1059–81.
60. Howard J, Hyman AA. Dynamics and mechanics of the microtubule plus end. Nature. 2003; 422:753–8. [PubMed: 12700769]
61. Hong TT, Smyth JW, Gao D, Chu KY, Vogan JM, Fong TS, et al. BIN1 Localizes the L-Type Calcium Channel to Cardiac T-Tubules. PLoS Biol. 2010; 8:1–14.
62. von Knethen A, Callsen D, Brune B. Superoxide attenuates macrophage apoptosis by NF-kappa B and AP-1 activation that promotes cyclooxygenase-2 expression. J Immunol. 1999:163.
63. Kukielka GL, Smith CW, Manning AM, Youker KA, Michael LH, Entman ML. Induction of interleukin-6 synthesis in the myocardium. Potential role in postreperfusion inflammatory injury. Circulation. 199(92):1866–75.
64. Zadeh AD, Cheng Y, Xu H, Wong N, Wang Z, Goonasekara C, et al. Kif5b is an essential forward trafficking motor for the Kv1.5 cardiac potassium channel. J Physiol. 2009; 587:4565–74. [PubMed: 19675065]
65. Arakel EC, Brandenburg S, Uchida K, Zhang H, Lin YW, Kohl T, et al. Tuning the electrical properties of the heart by differential trafficking of KATP ion channel complexes. J Cell Sci. 2014; 127:2106–19. [PubMed: 24569881]
66. Louch WE, Mork HK, Sexton J, Stromme TA, Laake P, Sjaastad I, et al. T-tubule disorganization and reduced synchrony of Ca2+ release in murine cardiomyocytes following myocardial infarction. J Physiol. 2006; 574:519–33. [PubMed: 16709642]

67. Lyon AR, MacLeod KT, Zhang Y, Garcia E, Kanda GK, Lab MJ, et al. Loss of T-tubules and other changes to surface topography in ventricular myocytes from failing human and rat heart. Proc Natl Acad Sci U S A. 2009; 106:6854–9. [PubMed: 19342485]

68. Brette F, Orchard CH. T-tubule function in mammalian cardiac myocytes. Circ Res. 2003; 92:1182–92. [PubMed: 12805236]

Highlights

- EB1 and EB3 associate in puncta along the length of MTs.
- MTs grow mainly perpendicular to T-tubules.
- MT dynamics are temperature dependent.
- Oxidative stress disrupts MT dynamics in cardiomyocytes during MI.
- MT destabilization reduces I_{to} by decreasing $\mathrm{K_V}$4.2 and $\mathrm{K_V}$4.3 surface expression.

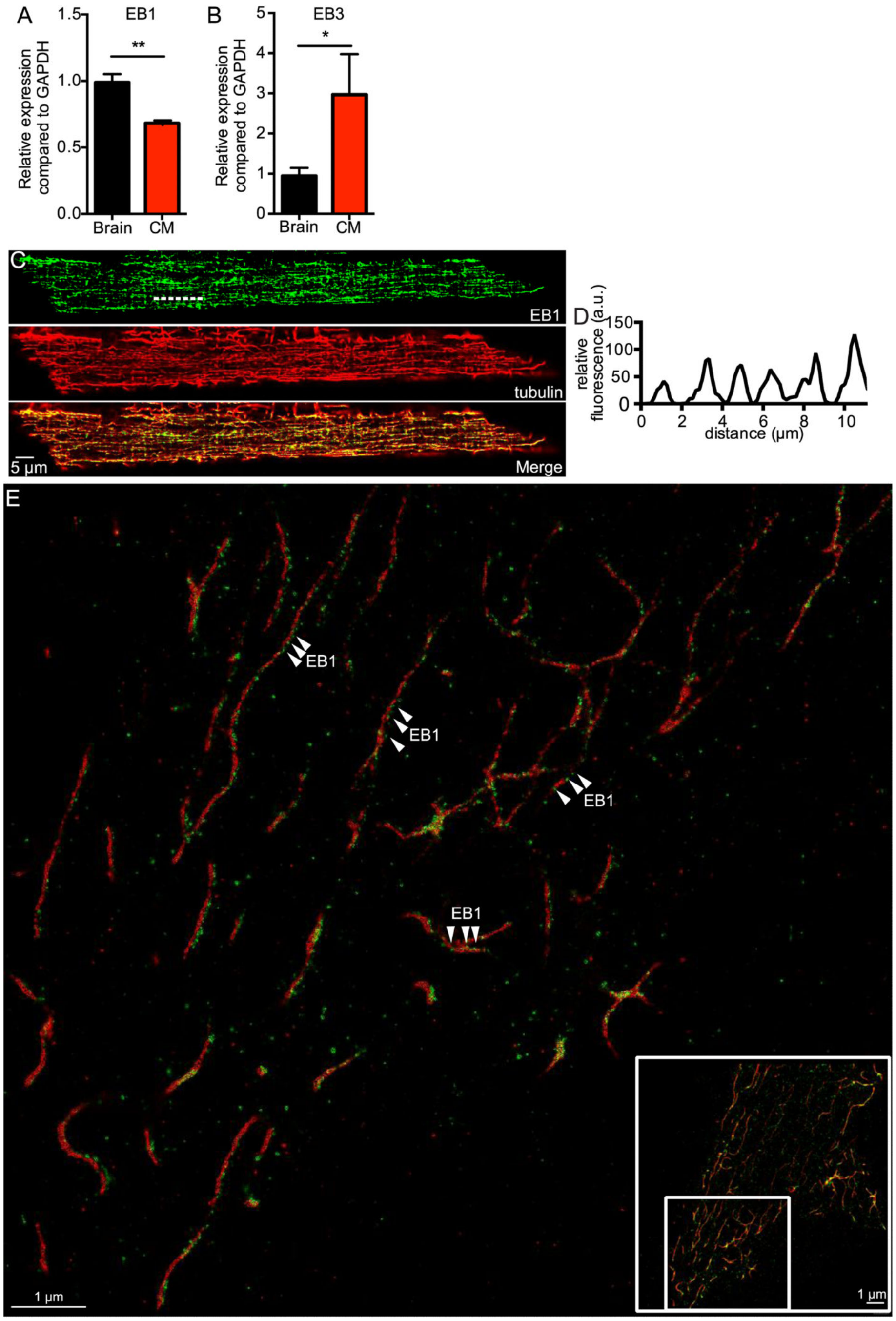

Fig. 1.

EB1 and tubulin co-localize in punctate pattern in ventricular myocytes. A, bar plot of the mean ± S.E.M. of relative real time qRT-PCR expression compared to GAPDH of EB1 in brain (*black*) and ventricular myocytes (*red*). B, bar plot of the mean ± S.E.M. of relative real time qRT-PCR expression compared to GAPDH of EB3 in brain (*black*) and cardiomyocytes (*red*). C, representative confocal image of a myocyte showing EB1 imaged with EGFP (*green*), tubulin imaged with RFP (*red*), and both signals merged, scale bar = 5 µm. D, fluorescent line profile of dashed line shown in EB1 signal of *C*, indicating Z-line periodicity. E, zoomed-in section of representative super-resolution image of myocyte showing tubulin stained with Alexa647 (*red*) and EB1 stained with Alexa568 (*green*) via a dual-antibody staining, scale bar = 1 μm. Arrowheads highlight prominent areas of punctate staining. Inset shows location of zoomed-in section in relation to full image, scale bar = 1 μm.

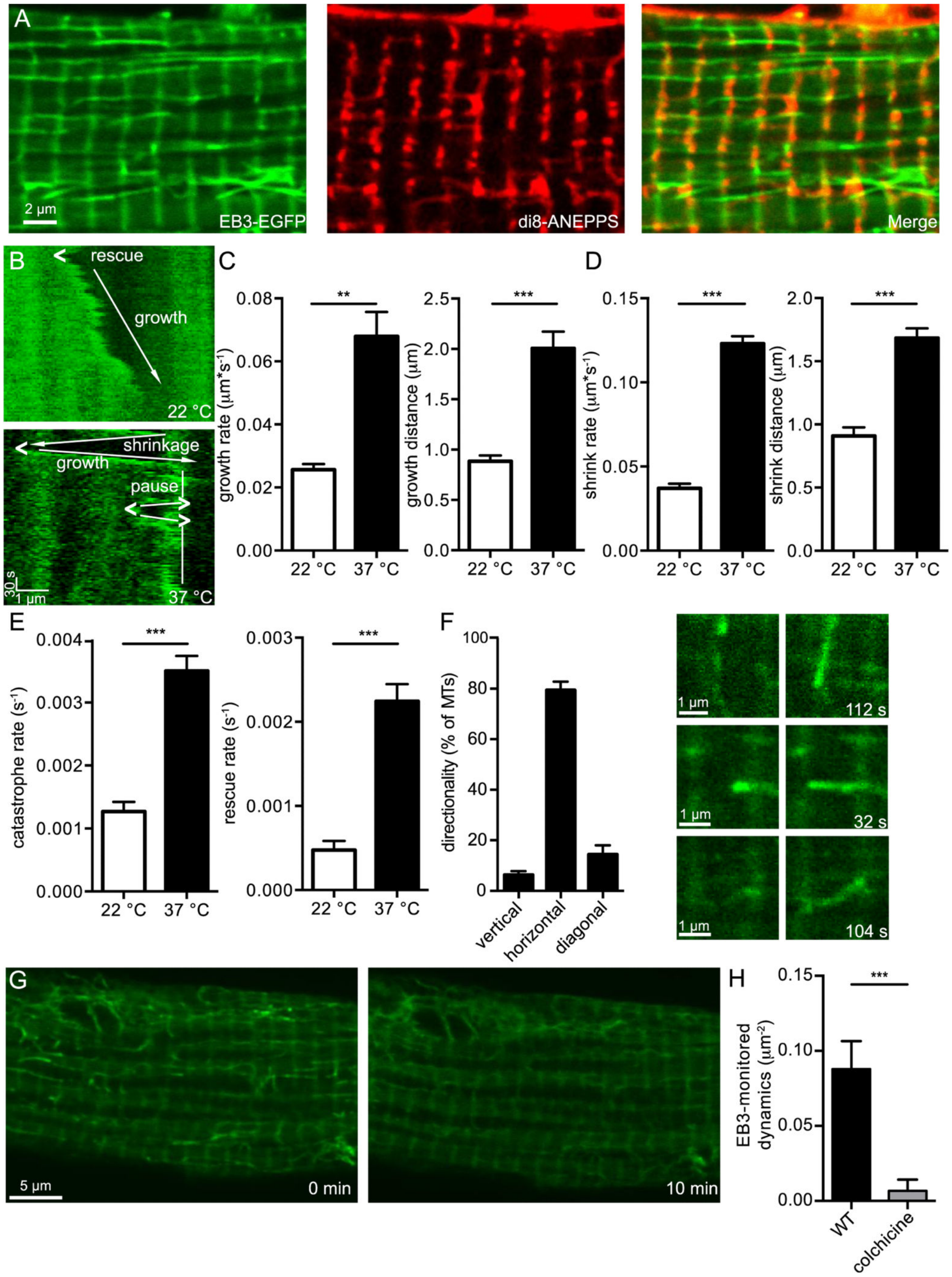

Fig. 2.

Live imaging of MTs in ventricular myocytes. A, representative 2D confocal image of a ventricular myocyte expressing Eb3-EGFP (*left*) and stained with di8-ANEPPS (*middle*), with overlaid signals (*right*), scale bar = 2µm. B, representative kymographs of a MT taken from a myocyte recorded at 22 °C (*above*) and a myocyte recorded at 37 °C (*below*), scale bars = 1µm horizontally and 30 s vertically. Growth directions indicated by arrows and rescue indicated by "<". The kymograph recorded from the MT at 37 °C also features a section of MT pausing, labeled with vertical line, and catastrophes indicated by ">". C, bar plots of the mean ± S.E.M. of average growth rate (*left*) and growth distance (*right*) of MTs from myocytes recorded at 22 °C (*white*) and cardiomyocytes recorded at 37 °C (*black*). D, bar plots of the mean ± S.E.M. of average shrink rate (*left*) and shrink distance (*right*) of MTs from cardiomyocytes recorded at 22 °C (*white*) and cardiomyocytes recorded at 22 °C (*black*). E, bar plots of the mean ± S.E.M. of average catastrophe rate (*left*) and rescue rate (*right*) of MTs from cardiomyocytes recorded at 22 °C (*white*) and myocytes recorded at 37 °C (*black*). F, bar plot of the percentage of MTs moving vertically (*vertical bars*), horizontally (*horizontal bars*), or diagonally *(diagonal bars*) (*left*) to the longitudinal axis of the cell, and representative examples of each type of movement. The first column of images is taken from start of cell recording, while the time points of the second column are indicated on the lower right in seconds. Scale bar = 1μm. G, representative confocal image of a myocyte before (*left*) and after (*right*) application of colchicine, scale bar = 5 μm. H, bar plot of the mean ± S.E.M. of the average EB3-monitored dynamics of cardiomyocytes before (*black*) and after (*gray*) 10 min application of colchicine.

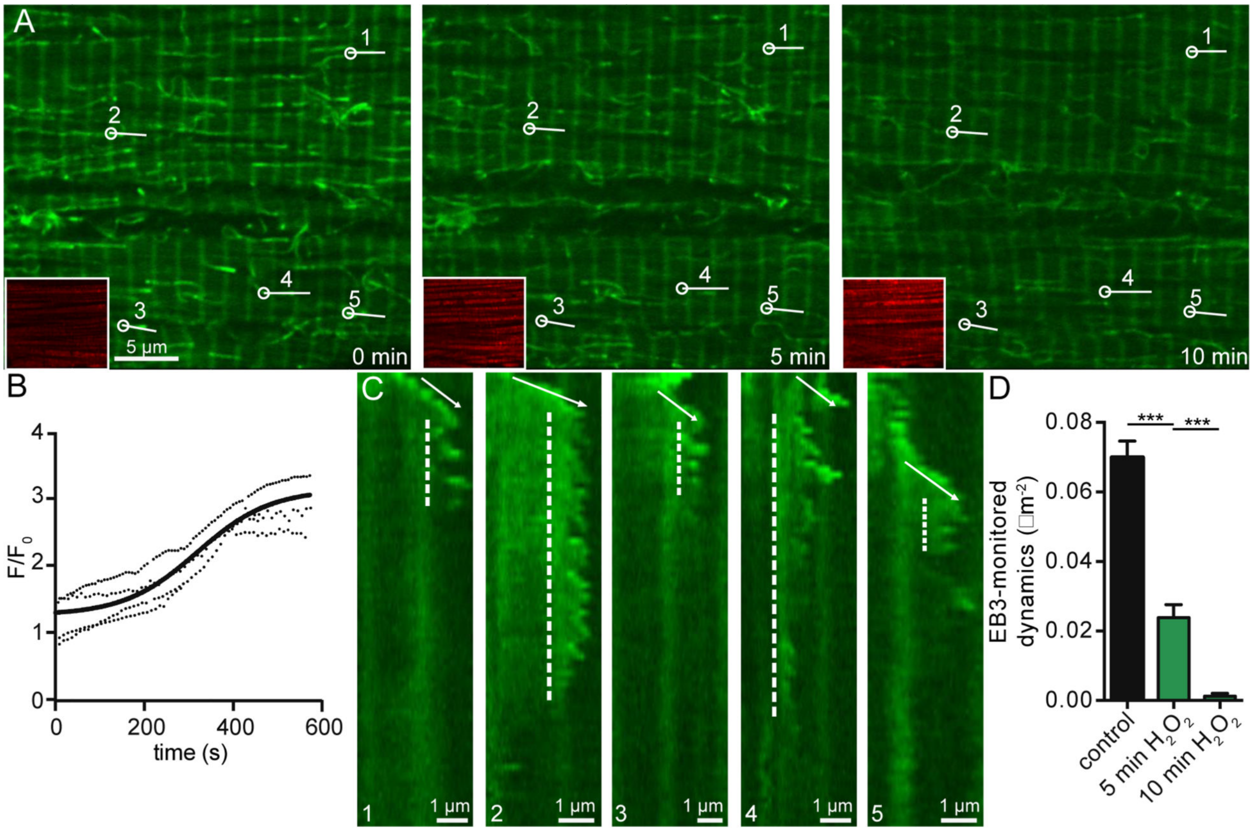

Fig. 3.

Oxidative stress disrupts MT dynamics. A, representative confocal images of a cell before (*left*) and after 5 min (*center*) and 10 min (*right*) application of 200 µM H_2O_2, scale bar = 5 µm. Lower left inset shows MitoSox Red channel. Numbers and lines indicate MTs shown in kymographs in C. B, representative plots of MitoSox Red fluorescence over time upon application of 200 µM H_2O_2 fit to sigmoidal curve. C, five kymographs of MTs over 10 min application. Entire kymograph image is 10 min, scale bar = 1 µm. Regions of growth are indicated by arrows and regions of instability by dashed lines. D, bar plot of the mean ± S.E.M. of average EB3-monitored dynamics of cardiomyocytes before (*black*) and after 5 min (*green*) and 10 min (*dark green*) application of 200 µM H_2O_2.

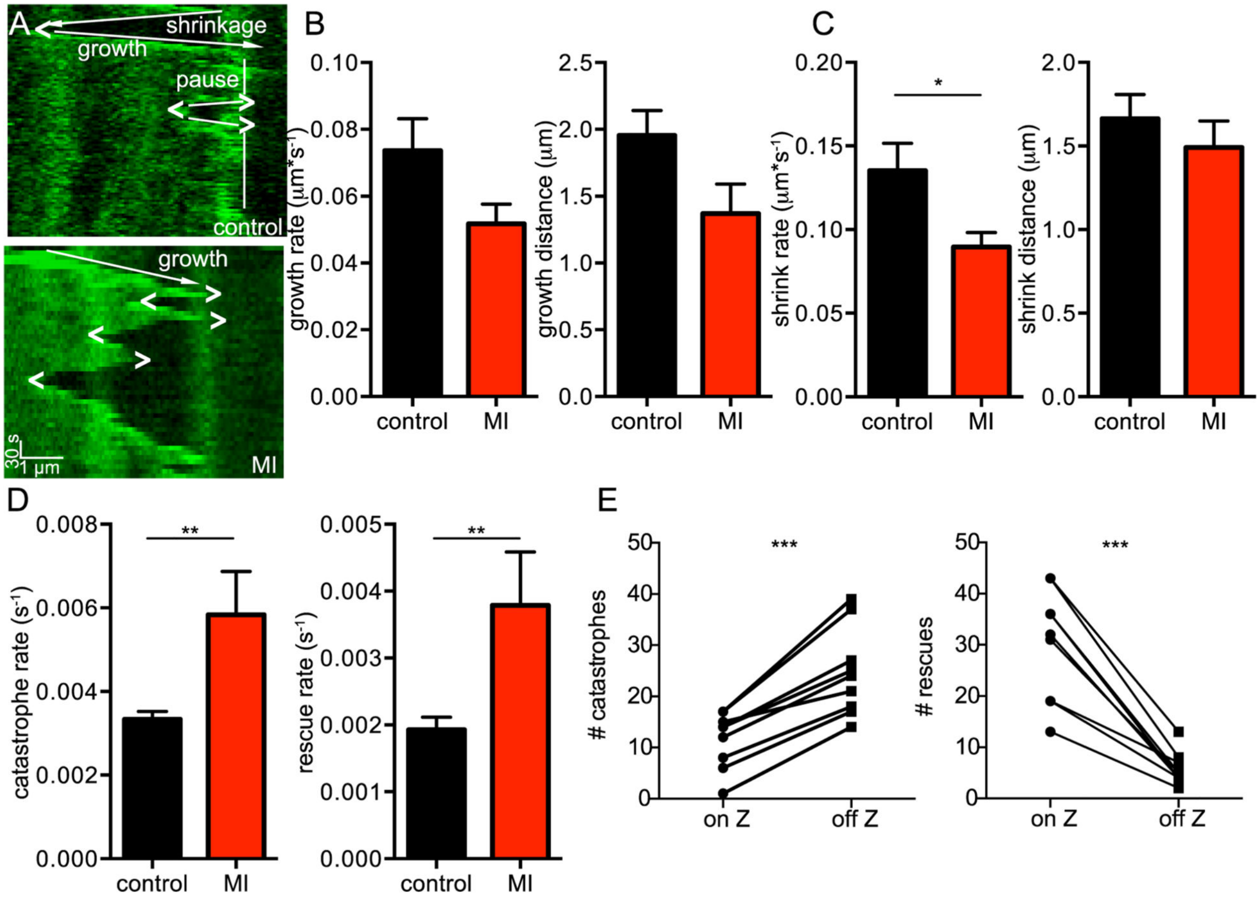

Fig. 4.

Live imaging of MTs in ventricular myocytes post-myocardial infarction. A, representative kymographs of a MT taken from a control myocyte (*above*) and an infarcted myocyte (*below*), scale bars = 1μm horizontally and 30 s vertically. Growth directions indicated by arrows, pausing by vertical line, catastrophes indicated by ">", and rescues indicated by "<". B, bar plots of the mean ± S.E.M. of average growth rate (*left*) and growth distance (*right*) of MTs from control (*black*) and infarcted (*red*) cells. C, bar plots of the mean ± S.E.M. of average shrink rate (*left*) and shrink distance (*right*) of MTs from control (*black*) and infarcted (*red*) cells. D, bar plots of the mean ± S.E.M. of average catastrophe rate (*left*) and rescue rate (*right*) of MTs from control (*black*) and infarcted (*red*) cells. E, bar plots tracking paired responses for each cell of the number of catastrophes (*left*) and rescues (*right*) occurring on and off of the Z-line.

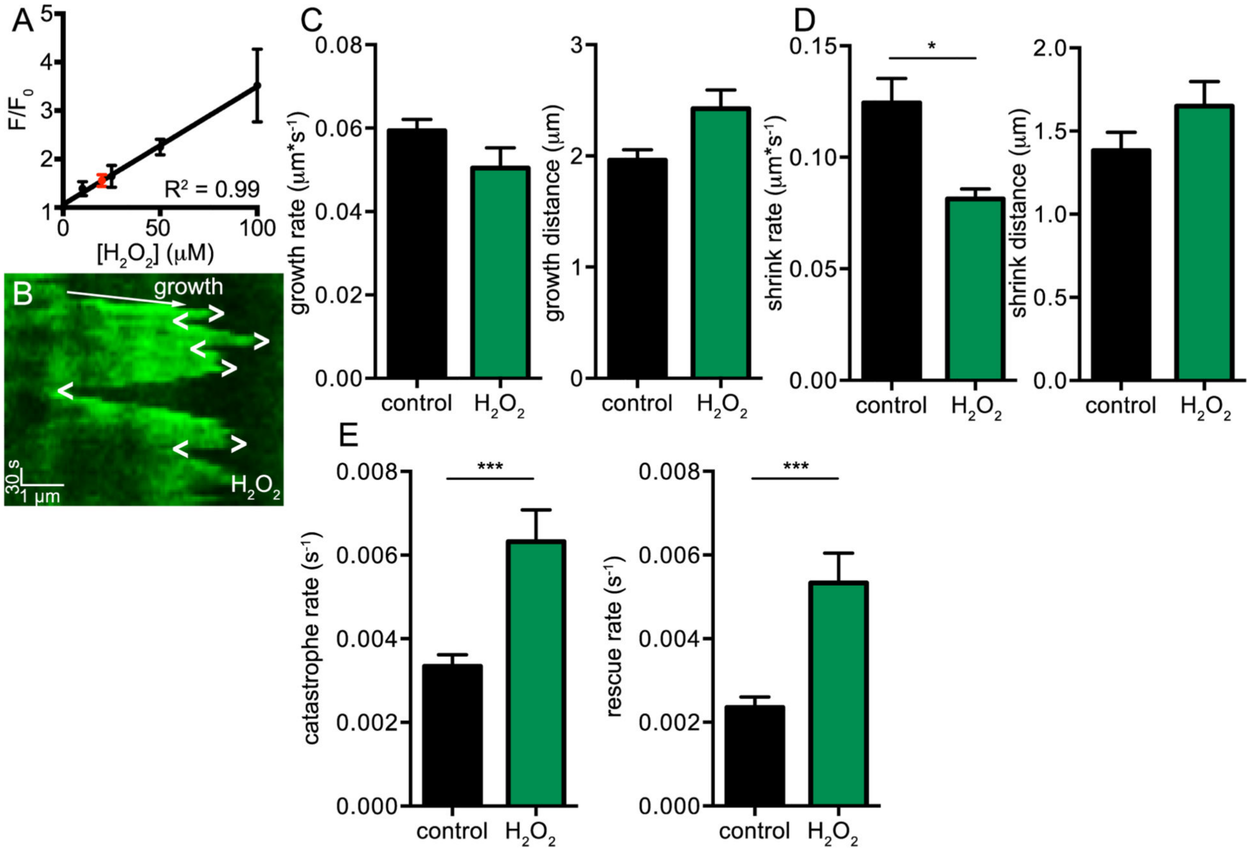

Fig. 5.

Oxidative stress mimics MT dynamic disruptions seen after MI. A, x-y plot of the mean ± S.E.M. of the relative fluorescence of MitoSox Red signal of cardiomyocytes exposed to various concentrations of H_2O_2 fit to linear model. Red circle shows mean ± S.E.M. of relative fluorescence of cardiomyocytes from MI model. B, representative kymograph of MT imaged from cardiomyocyte exposed to 10 μM H_2O_2, scale bars = 1μm horizontally and 30 s vertically. Growth directions indicated by arrow, catastrophes indicated by ">", and rescues indicated by "<". C, bar plots of the mean ± S.E.M. of average growth rate (*left*) and growth distance (*right*) of MTs from control cells (*black*) and cells treated with 10 μM H_2O_2 (*green*) cells. D, bar plots of the mean ± S.E.M. of average shrink rate (*left*) and shrink distance (*right*) of MTs from control cells (*black*) and cells treated with 10 μM H_2O_2 (*green*) cells. E, bar plots of the mean ± S.E.M. of average catastrophe rate (*left*) and rescue rate (*right*) of MTs from control cells (*black*) and cells treated with 10 μM H_2O_2 (*green*) cells.

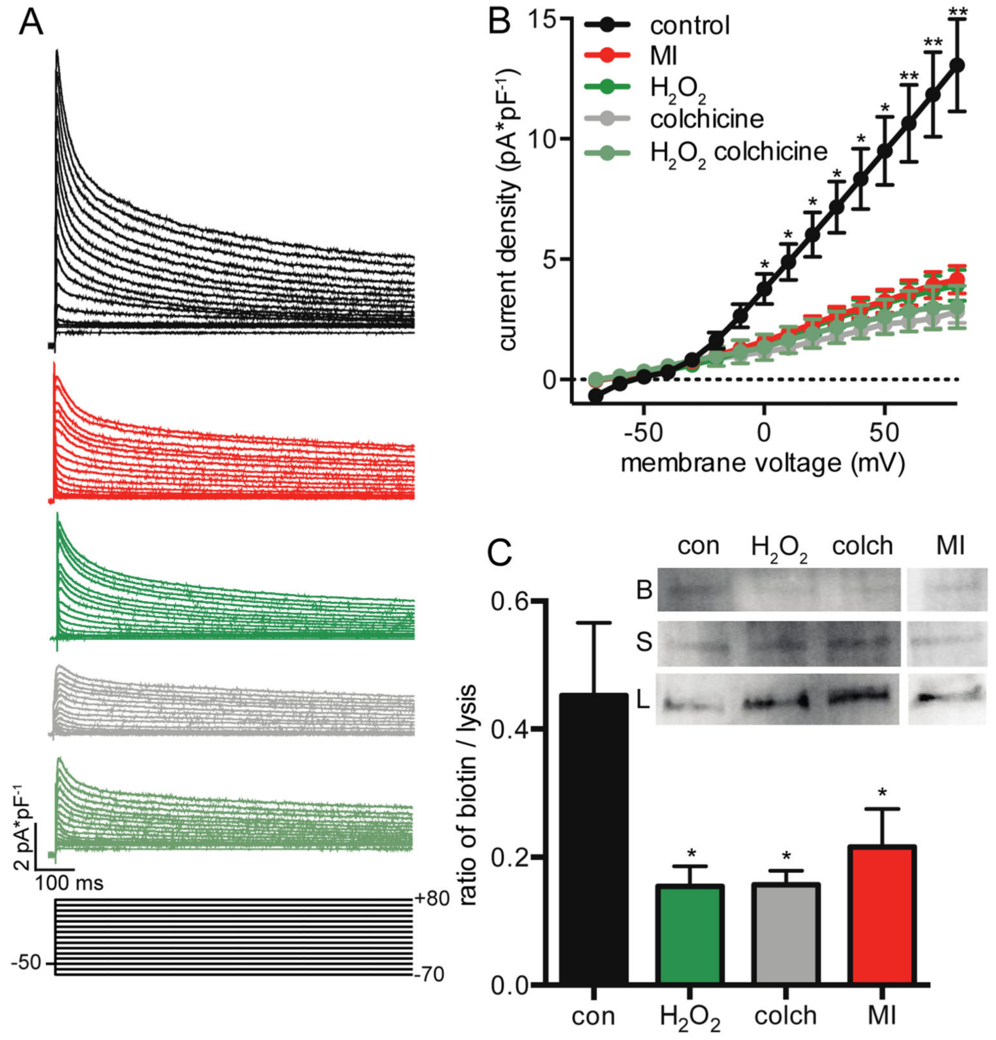

Fig. 6.

Reduction in Kv4 trafficking from MT disruption. A, representative currents from mouse cardiomoyocytes under control conditions (*black*), after infarct (*red*), and after treatment with H_2O_2 (*dark green*), colchicine (*gray*), and both H_2O_2 and colchicine (*green-gray*). Scale bars = 100 ms horizontally and 2 pA*pF^{-1} vertically. Voltage protocol shown below, 10 mV separating each line. B, x-y plot of the mean ± S.E.M. of the average current density of control, infarcted, H_2O_2, colchicine, and colchicine + H_2O_2 treated cells for a given voltage. C, bar plot of the mean ± S.E.M. of the average surface expression of $K_v4.2$ and $K_v4.3$ channels under control conditions, after 4 hour treatment with H_2O_2, after 4 hour treatment with colchicine, and from infarcted cells. Inset shows representative Western blot. B indicates biotinylated band, S indicated supernatant band, and L indicates lysis band. Lane 1 is control (*con*), lane 2 treated with H_2O_2 (*H_2O_2*), lane 3 treated with colchicine (*colch*) and lane 4 infarcted (*MI*).